NANO LETTERS

Letter

pubs.acs.org/NanoLett

In Situ Transmission Electron Microscopy Study of Electrochemical Sodiation and Potassiation of Carbon Nanofibers

Ying Liu,[†] Feifei Fan,[‡] Jiangwei Wang,[§] Yang Liu,[∥] Hailong Chen,[‡] Katherine L. Jungjohann,[∥] Yunhua Xu,[†] Yujie Zhu,[†] David Bigio,[⊥] Ting Zhu,[‡,*] and Chunsheng Wang[†,*]

[†]Department of Chemical and Biomolecular Engineering, University of Maryland, College Park, Maryland 20742, United States

[‡]Woodruff School of Mechanical Engineering, Georgia Institute of Technology, Atlanta, Georgia 30332, United States

[§]Department of Mechanical Engineering and Materials Science, University of Pittsburgh, Pittsburgh, Pennsylvania 15261, United States

[∥]Center for Integrated Nanotechnologies, Sandia National Laboratories, Albuquerque, New Mexico 87185, United States

[⊥]Department of Mechanical Engineering, University of Maryland, College Park, Maryland 20742, United States

Supporting Information

ABSTRACT: Carbonaceous materials have great potential for applications as anodes of alkali-metal ion batteries, such as Na-ion batteries and K-ion batteries (NIB and KIBs). We conduct an in situ study of the electrochemically driven sodiation and potassiation of individual carbon nanofibers (CNFs) by transmission electron microscopy (TEM). The CNFs are hollow and consist of a bilayer wall with an outer layer of disordered-carbon (*d*-C) enclosing an inner layer of crystalline-carbon (*c*-C). The *d*-C exhibits about three times volume expansion of the *c*-C after full sodiation or potassiation, thus suggesting a much higher storage capacity of Na or K ions in *d*-C than *c*-C. For the bilayer CNF-based electrode, a steady sodium capacity of 245 mAh/g is measured with a Coulombic efficiency approaching 98% after a few initial cycles. The in situ TEM experiments also reveal the mechanical degradation of CNFs through formation of longitudinal cracks near the *c*-C/*d*-C interface during sodiation and potassiation. Geometrical changes of the tube are explained by a chemomechanical model using the anisotropic sodiation/potassiation strains in *c*-C and *d*-C. Our results provide mechanistic insights into the electrochemical reaction, microstructure evolution and mechanical degradation of carbon-based anodes during sodiation and potassiation, shedding light onto the development of carbon-based electrodes for NIBs and KIBs.

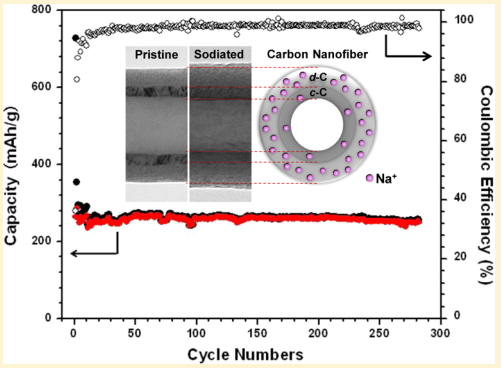

KEYWORDS: *Sodium-ion batteries, potassium-ion batteries, carbon nanofibers, sodiation, potassiation, crack*

The large-scale storage of electrical energy for applications in electrical grids requires battery systems with high energy density and low cost. During the past decade, great effort has been devoted to Li-ion batteries (LIBs).[1,2] However, the limited energy density and high cost still hinder the wide usage of LIBs to store large amounts of electrical energy from intermittent renewable sources such as solar and wind energy. Recently, batteries based on other alkali-metals, such as Na-ion batteries (NIBs) and K-ion batteries (KIBs),[3−5] have attracted great attention, owing to their comparatively high natural abundance and low cost.[3,5−7] Considering the similar chemical properties of Li, Na, and K, the anode and cathode materials used in LIBs are being investigated for their applications in NIBs and KIBs in the past few years.

The potential anode materials for NIBs include carbonaceous materials, Sn, Sb, and metal oxides.[3,6−12] Among these candidates, carbonaceous materials[4,13−19] are most promising, given their successful applications in commercial LIBs and particularly low cost, natural abundance, and small volumetric expansion during alloying with alkali-metals, in contrast to other anode materials such as Sn.[10] Graphite has been used as the anode of current commercial LIBs with a theoretical capacity of 372 mAh/g.[20] However, only a small amount of Na ions can be stored in the graphite anode of NIBs. Such a limitation has been often attributed to the higher intercalation energy barrier of Na ions.[3,4,21] So far, the highest capacity for carbonaceous anodes reported in NIBs is about 300 mAh/g in hard carbon, whose usage is severely limited by its poor cyclability.[19] Recently, the disordered or amorphous carbon materials were found to exhibit much improved cyclability.[4,15,22] For example, the disordered hollow carbon nanowires showed a reversible capacity as high as 251 mAh/g with 82.2% capacity retention after almost 400 sodiation-desodiation cycles,[15] which is much better than hard carbon.[16,19] Moreover, carbon is often used to enhance electron

Received: March 14, 2014
Revised: May 10, 2014
Published: May 13, 2014

   dx.doi.org/10.1021/nl500970a | *Nano Lett.* 2014, 14, 3445−3452

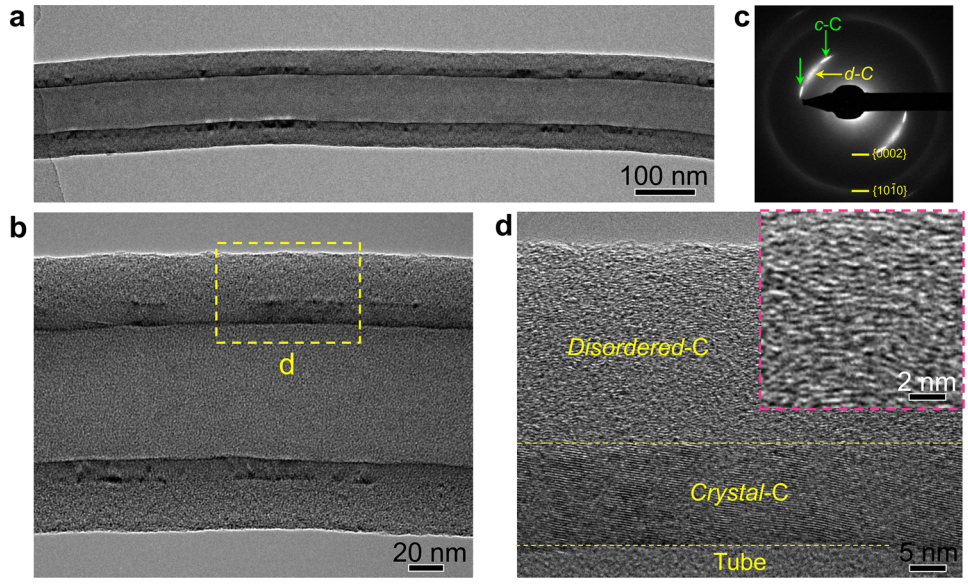

Figure 1. Typical morphology and structure of a pristine hollow CNF with a bilayer wall. (a,b) The wall of CNF consists of a *d*-C/*c*-C bilayer. (c) EDP of the bilayer CNF. Two different kinds of spots are shown in the EDP for the {0002} plane of CNF. The two sets of sharp spots (indicated by green arrows) correspond to the diffraction of *c*-C, while the diffuse spots (indicated by yellow arrows) correspond to the diffraction of *d*-C. (d) HRTEM image of the CNF with the inset showing the local graphite lattice fringes in the *d*-C layer.

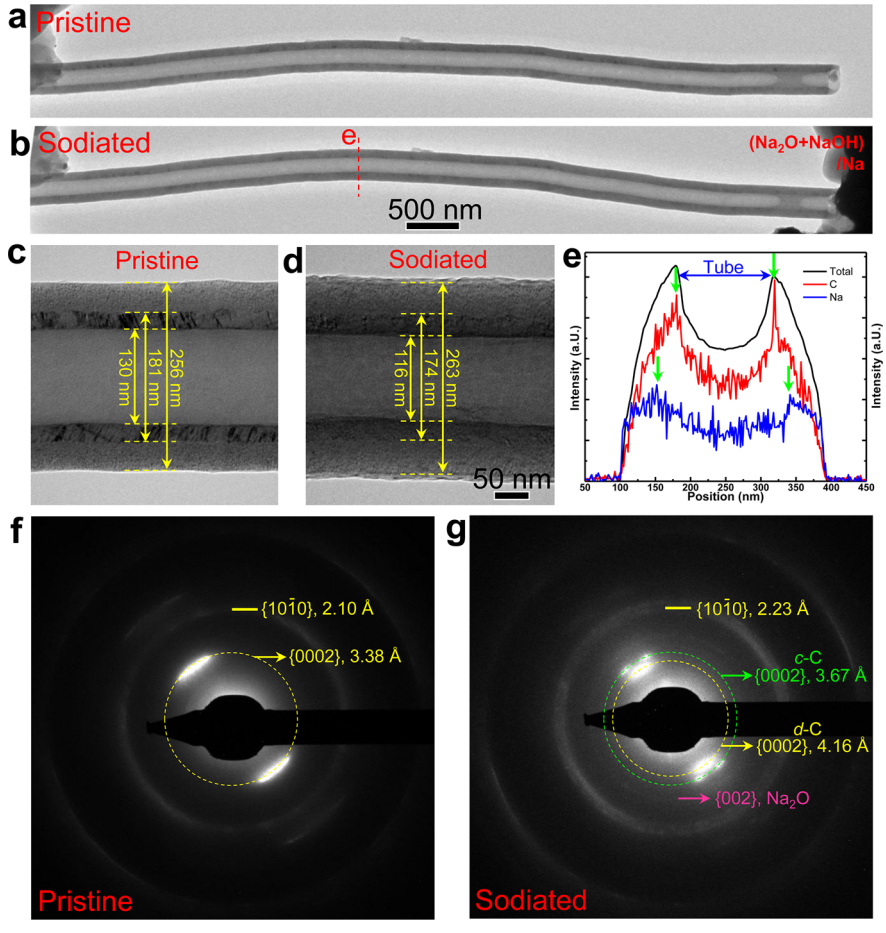

Figure 2. Geometry and structure changes of a bilayer CNF during sodiation under a beam-blank condition. (a,c) Pristine CNF. (b,d) Sodiated CNF. (e) The line scan profiles of C and Na across the CNF after sodiation. The green arrows point to the peak positions of Na and C intensity profiles. (f,g) Electron diffraction patterns (EDPs) of the CNF before and after sodiation. The average spacing of {0002} planes is about 3.38 Å in the pristine CNF. Two sets of patterns form after sodiation; the average spacing of {0002} planes in *c*-C and *d*-C increases to 3.67 and 4.16 Å, respectively.

dx.doi.org/10.1021/nl500970a | *Nano Lett.* 2014, 14, 3445−3452

conduction in anodes or cathodes of LIBs and NIBs, as well as to support other active materials in high-capacity nanocomposite anodes for LIBs and NIBs.[23−29] In addition, the application of the carbon-based anodes in KIBs remains largely unexplored, compared with their LIB and NIB counterparts. Therefore, it is essential to understanding the electrochemical reactions and associated structure−property relationships of carbon-based anodes during sodiation and potassiation, thereby paving the way for future development of the novel carbon-based or carbon-supported nanocomposite anodes for NIBs and KIBs.

In this work, the electrochemical behavior and microstructure evolution of carbon nanofibers (CNFs) during Na^+ and K^+ insertions are studied in real time by using a nanoscale battery setup inside a transmission electron microscope (TEM). The CNFs are hollow and consist of a bilayer wall with an outer layer of disordered-carbon (*d*-C) enclosing an inner layer of crystalline-carbon (*c*-C). With such bilayer CNFs, the sodiation and potassiation responses of *c*-C and *d*-C are directly compared. Longitudinal cracks are frequently observed near the *c*-C/*d*-C interface during sodiation and potassiation. The chemo-mechanical origin of geometrical changes in the sodiated tube is revealed by a computational modeling study. In addition, an in situ TEM study of amorphous Si (*a*-Si) coated CNFs is conducted to further evaluate the mechanical confinement effect on sodiation and potassiation.

Figure 1 shows the typical morphology of a pristine hollow CNF, which involves a bilayer structure, that is, a *d*-C outer layer enclosing a *c*-C inner layer. The bilayer CNF is a commercial product (PR-19) ordered from the Pyrograf Products, Inc. The diameter of CNFs is typically in the range of 120−300 nm and the length is about tens of micrometers. The bilayer structure is clearly seen from a zoom-in image in Figure 1b, that is, the *c*-C inner layer with a dark contrast and the *d*-C outer layer with a light contrast. Figure 1d shows a high-resolution TEM (HRTEM) image of the bilayer structure. In the *d*-C layer, the local domains of graphitic lattice fringes (inset in Figure 1d) are clearly visible, implying *d*-C is not completely disordered. Namely, *d*-C consists of an assembly of many few-layered graphene patches that are not perfectly aligned in the same orientation. Such a locally ordered structure in *d*-C is similar to that in hard carbon consisting of stacked graphite layers (termed as graphite nanocrystallites) with microvoids in between.[19,21] The local crystalline order in *d*-C is also reflected in the electron diffraction pattern (EDP), as shown in Figure 1c. It is interesting to note that two different kinds of spots are shown in the EDP for {0002} planes. The two sets of sharp spots (indicated by green arrows in Figure 1c) arise from the diffraction of *c*-C, while the diffuse spots from *d*-C (indicated by the yellow arrow in Figure 1c). Note that the diffuse diffraction spots of *d*-C are different from the diffraction halo of the pure amorphous phase, which further confirms that the *d*-C layer is not fully disordered. The unique bilayer structure in CNFs allows us to directly compare the behaviors of *c*-C and *d*-C during Na^+ or K^+ insertion.

The in situ experiments of electrochemically driven sodiation and potassiation of CNFs are conducted by using an all-solid nanobattery setup inside a TEM, and details of the nanobattery setup and operation can be found in previous publications.[10,29−32] To confirm the negligible effects of electron beam on electrochemical reactions, both beam-on and beam-blank experiments (as indicated in figure captions) are performed, showing qualitatively similar behaviors. Figure 2 presents the microstructures of a hollow bilayer CNF before and after the beam-blank sodiation. For the pristine hollow CNF, its inner and outer diameter are respectively 130 nm and 256 nm, and wall thickness is about 63 nm (Figure 2c). After full sodiation, the inner diameter decreases to 116 nm and the outer diameter increases to 263 nm. As a result, the total wall thickness increases to 73.5 nm, owing to sodiation-induced volume expansion. In addition, sodiation causes an increase of the thickness of the *c*-C layer from 25.5 to 29 nm, which corresponds to an average radial and volume strain of 13.7 and 6%, respectively. Similarly, the thickness of the *d*-C layer increases from 37.5 to 44.5 nm, which corresponds to an average radial and volume strain of 18.7 and 18.7%, respectively. Similar geometric changes are also observed in potassiated CNFs. Hence, the sodiated/potassiated *d*-C exhibits about three times volume expansion of *c*-C, thus suggesting a much higher storage capacity of Na ions in *d*-C than *c*-C. Incidentally, a thin layer of Na_2O (2−3 nm thick) is observed to quickly form on the CNF surface (Figure 2d) while the bulk sodiation is still ongoing, thus suggesting fast surface diffusion of Na on CNFs.[30,31]

Figure 2e presents the line scan profiles across the CNF after sodiation, and the green arrows indicate the peak positions of Na and C intensity profiles. Na and C exhibit different spatial distributions, that is, the Na intensity reaches a peak in the middle of the CNF wall and decreases gradually away from the peak, while the C intensity continually increases from the outer to the inner tube wall. Such difference indicates that the *c*-C and *d*-C have different capacities of storing Na ions, as further confirmed by EDPs (Figure 2f,g). The EDP of the pristine CNF shows a typical diffraction pattern of the bilayer CNF with an average {0002} plane spacing of 3.38 Å (Figure 2f), which is slightly larger than the theoretical spacing of {0002} plane of 3.35 Å. Such a difference is presumably induced by the partially disordered structure of *d*-C. After full sodiation, the diffraction pattern of {0002} planes splits into two sets with different lattice spacings (Figure 2g). For *c*-C, the average spacing of {0002} planes increases to 3.67 Å. This corresponds to an expansion of 8.6% between neighboring graphitic layers, which is slightly larger than that of lithiation (~7%)[31] and can be correlated to the larger size of Na ions.[3] In contrast, the average spacing of {0002} planes of *d*-C increases up to about 4.16 Å. This corresponds to an expansion of ~23% along [0002] (i.e., *c* axis) direction, which is about three times that in the sodiated *c*-C. The larger the increase of the *d*-spacing along *c* axis, the more Na ions the carbon system likely stored. However, the quantitative capacity of sodiation in *d*-C cannot be determined directly by our in situ TEM experiment due to the difficulty of measuring the extremely small electric current. In addition, much less changes are observed in the lattice spacing of $\{10\bar{1}0\}$ planes (Figure 2f,g), which indicates that Na ions are most likely inserted in between rather than within the graphitic layers. The EDP after sodiation is consistent with the line scan profiles in Figure 2e, suggesting that more Na ions can be stored in *d*-C. Compared to *c*-C, the larger capacity of Na ions storage in *d*-C might originate from more defects existing in *d*-C, while the atomic-scale mechanism of Na ion accommodation warrants further study in the future. Potassiation of a bilayer CNF exhibits similar responses, as shown in Supporting Information Figure S1. The average spacing of {0002} planes of *d*-C increases to ~4.18 Å after potassiation, corresponding to an expansion of ~24% along the *c*-axis. Both sodiation and potassiation of the bilayer CNF indicate that *d*-C has a better capability of storing Na or K ions than *c*-C, which is desired for the anode of NIBs and KIBs.

Galvanostatic discharge−charge cycling is performed to directly measure the capacity of the bilayer CNF electrode

dx.doi.org/10.1021/nl500970a | *Nano Lett.* 2014, 14, 3445−3452

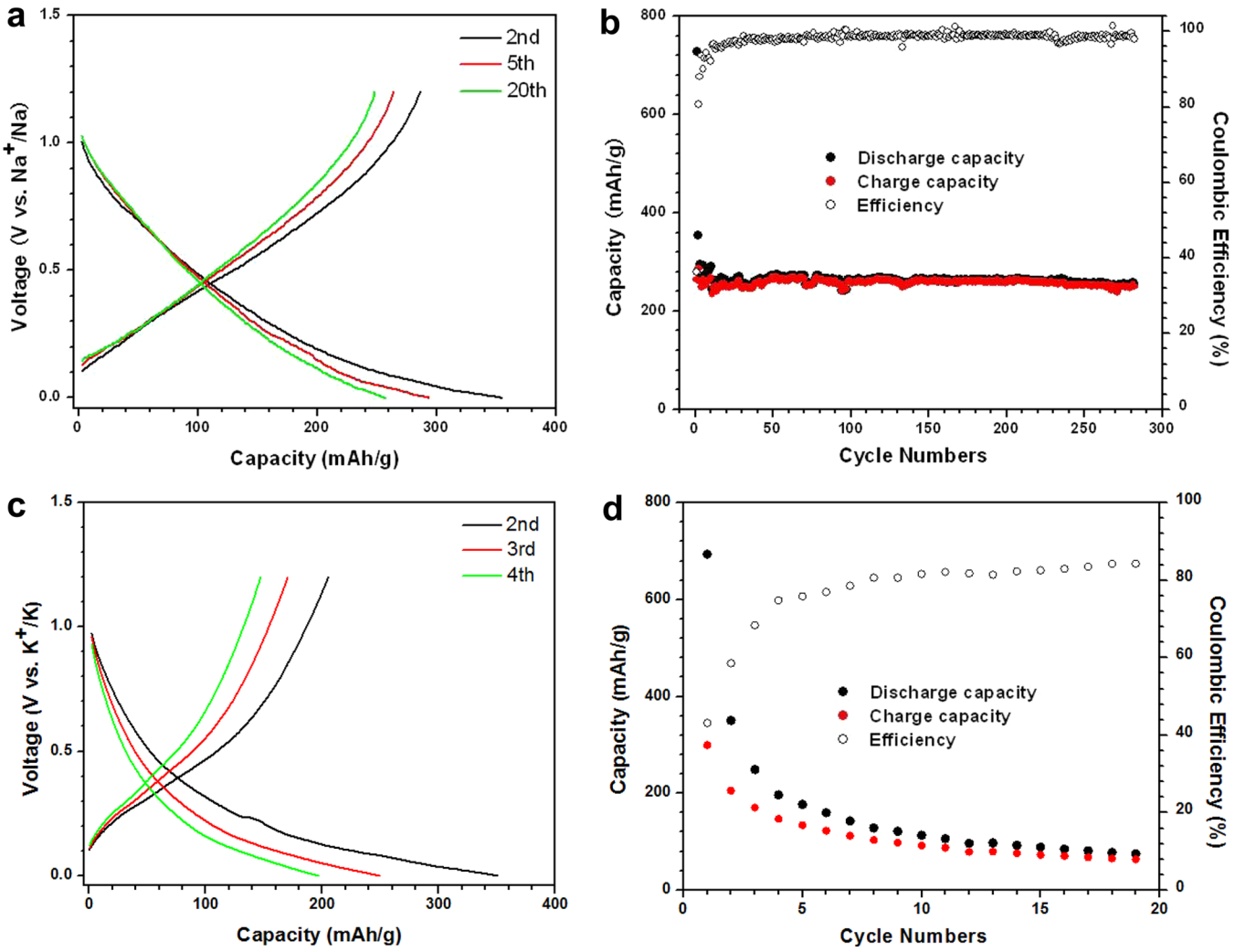

Figure 3. Charge−discharge curves and cycling stability measured for bilayer CNF electrodes in a coin cell for Na-ion battery and K-ion battery. The electrodes are tested in the voltage range of 0−1.2 V at a current density of 50 mA/g, with the electrolyte of 1 M $NaPF_6$ or 1 M KPF_6 dissolved in the mixture of EC + DMC (1:1 by volume). The specific capacity is calculated based on the mass of *d*-C, which is about 75% of the total mass of CNFs. (a) Galvanostatic charge−discharge profiles in the second, fifth, and twentieth cycle in NIBs. (b) Cycling performance and Coulombic efficiency of bilayer CNF electrodes in NIBs. (c) Galvanostatic charge−discharge profiles in the second, third, and fourth cycle in KIBs. (d) Cycling performance and Coulombic efficiency of bilayer CNF electrodes in KIBs.

during sodiation and desodiation at a constant current rate of 50 mA/g in a coin cell (Figure 3); experimental details are provided in the Supporting Information. The capacity of *c*-C during Na insertion/extraction was reported to be extremely small.[21] For bilayer CNFs, our in situ TEM electrochemical studies indicated that Na ions are mainly stored in *d*-C rather than *c*-C, based on the different volume changes upon sodiation. Hence, the specific capacity is calculated based on the weight of *d*-C only, which accounts for about 75% of the total mass of CNFs, as estimated from the average thicknesses of *d*-C and *c*-C layers for more than 30 samples. For sodiation of the carbon-based anodes, previous studies indicate that there are two dominant mechanisms of Na insertion: (1) insertion of Na between the graphene layers corresponding to the sloping voltage profile; (2) insertion of Na into the micropores corresponding to a plateau at a low potential.[4] In this work, because the micropores in bilayer CNFs are limited, the discharge−charge curve in Figure 3a exhibits a sloping profile in the voltage range of 0 to 1.2 V, which likely corresponds to the insertion of Na ions between the graphene layers in *d*-C.[4] This is consistent with our TEM results in Figure 2f,g, where Na ions insert in between the graphene layers of stacked graphite patches in *d*-C.[15] Figure 3b shows the capacity stability and Coulombic efficiency during Na insertion and extraction. The initial discharge and charge capacities are 728 and 263 mAh/g, respectively, giving a Coulombic efficiency of 36%. The large irreversible capacity in the first cycle is likely due to electrolyte decomposition to form the solid electrolyte interphase (SEI) at the electrode surface, as well as irreversible insertion of Na into graphitic layers. The capacity decay occurs primarily in the first few cycles, which is possibly attributed to the SEI stabilization, volume adjustment during Na ions insertion/extraction and partially irreversible Na ions insertion.[4,15] After initial adjustment cycles, a reversible capacity of 245 mAh/g is maintained with a Coulombic efficiency approaching 98%, which is in good agreement with other reported results on sodiated disordered carbon.[15,33] Since the inactive *c*-C can function as a built-in current collector, this bilayer CNF electrode shows excellent cycling stability with 99% capacity retention after 280 cycles, indicating a great potential of *d*-C in the application for NIBs. In addition, the bilayer CNF electrode also exhibits a

dx.doi.org/10.1021/nl500970a | *Nano Lett.* 2014, 14, 3445−3452

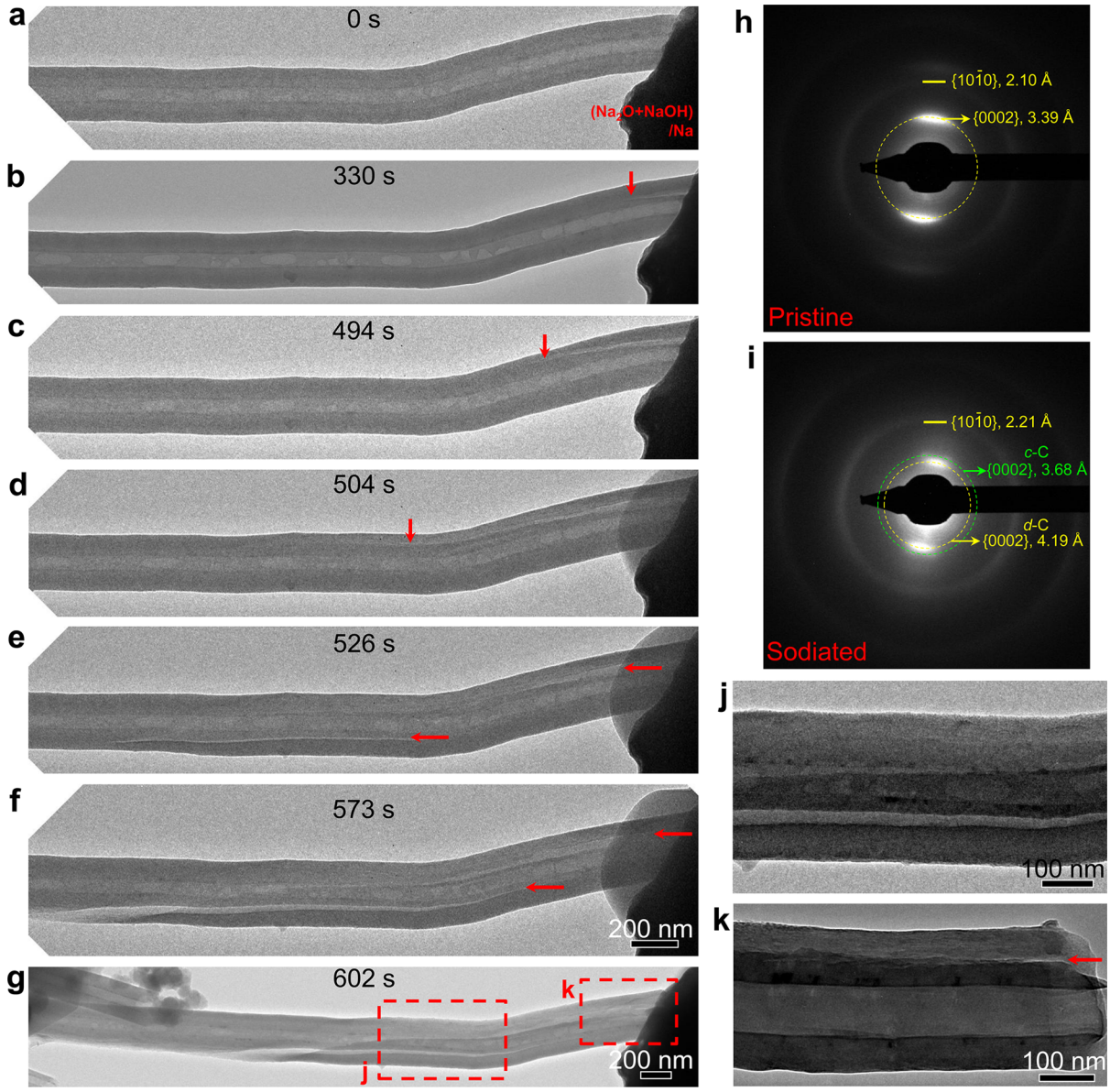

Figure 4. Sodiation-induced crack nucleation and propagation in a hollow bilayer CNF. The experiment was conducted under a beam-on condition with very weak electron-beam exposure. (a) Pristine CNF. (b−g) The dynamic process of the sodiation-induced crack nucleation and propagation. Upon sodiation, a crack is observed to nucleate from the contact point between the CNF and Na_2O/Na electrolyte, and it extends from one end to the other end along the longitudinal direction. The red arrows indicate the crack and its propagation front. (h,i) EDPs of the CNF before and after the sodiation. (j,k) Zoom-in images showing the cracks close to the *c*-C/*d*-C interface.

similar sloping profile in the discharge/charge curve in K-ion batteries at the same current rate of 50 mA/g in the voltage range of 0−1.2 V, as shown in Figure 3c. Similar to NIBs, the sloping discharge/charge curve likely corresponds to the insertion of K ions between graphene layers in *d*-C, which is supported by the TEM results in Supporting Information Figure S1c,d. However, Figure 3d shows that the cycle stability of the bilayer CNF electrode for KIBs is not as good as for NIBs, possibly due to the relatively slow kinetics of large K ions. Nonetheless, both our electrochemical testing and in situ TEM results suggest that *d*-C is a viable material for KIBs.

Mechanical degradation in electrodes is usually an important cause of the irreversible capacity loss in rechargeable batteries.[34] Our in situ TEM study reveals the mechanical degradation through formation of interface cracks in bilayer CNFs during sodiation and potassiation. Figure 4 shows an in situ TEM result of the sodiation-induced cracks in a bilayer CNF. The sample is tested under beam-on with a very weak electron beam. Upon sodiation, a crack nucleates from the contact point between the CNF and Na_2O/Na electrolyte, as indicated by red arrows in Figure 4b. As sodiation proceeds, the crack propagates from one end to the other end of the CNF along its axial direction (Figure 4c,d). Interestingly, the crack initially nucleates on the upper wall of the CNF and then extends to its lower wall, which is likely caused by screw rotation of the moving crack front around the axial direction (Figure 4e−g). Such kind of sodiation-induced cracking is frequently observed (5 out of 6 samples) with either beam-on or beam-blank (Figure 2 and Supporting Information Figures S1−3), thus suggesting the insensitivity of cracking to electron beam. Similar to Figure 2f,g, a large increase in the spacing of {0002} planes is observed after sodiation (Figure 4h,i). Figure 4j,k shows the zoom-in images of longitudinal

dx.doi.org/10.1021/nl500970a | *Nano Lett.* 2014, 14, 3445−3452

cracks, which are located at different places, but all close to the interface between the *c*-C and *d*-C layers. Supporting Information Figure S1 shows an in situ TEM result of potassiation of a bilayer CNF, where cracks near the interface are also observed. In contrast, no cracking is observed during the sodiation of monolithic *d*-C CNFs, being either solid or hollow, as shown in Supporting Information Figure S4. Such different cracking behaviors suggest that the unique bilayer structure, along with the hollow geometry, plays an important role in crack formation during sodiation and potassiation of CNFs. Such interface cracking might be responsible for capacity fading in the initial charge/discharge cycles in Figure 3.[30]

To understand the geometrical changes in CNFs, it is essential to elucidate the mechanism of strain generation and accommodation during sodiation (and potassiation). Particularly, one needs to explain the origin of the decreasing inner radius of the tube, as seen from Figure 2c,d. This result is somewhat counterintuitive, because one would expect that the sodiation-induced volume increase tends to cause an outward expansion of the tube that would result in an increase of the inner radius. To explain this unexpected result, we develop a continuum chemomechanical model to simulate the concurrent processes of Na diffusion and mechanical deformation. In the model, the strain at any material point ε_{ij} is assumed to consist of two parts, $\varepsilon_{ij} = \varepsilon^{c}_{ij} + \varepsilon^{m}_{ij}$, where ε^{c}_{ij} is the chemical strain induced by Na insertion under a stress-free condition and ε^{m}_{ij} is the elastic strain due to chemically induced mechanical deformation. The components of chemical strain ε^{c}_{ij} depend on the underlying atomic processes of Na insertion in *c*-C and *d*-C. A physical assignment of the appropriate values for ε^{c}_{ij} is critical to explain the sodiation-induced geometrical changes. We note that *c*-C consists of parallel graphene layers, and interlayer expansion is the primary deformation mode upon Na insertion. Hence, we assume the chemical strain ε^{c}_{ij} is highly anisotropic with only one nonzero component perpendicular to graphene layers, that is, in the radial direction of a CNF. Similarly, *d*-C consists of patches of few-layered graphene that are approximately aligned in the radial direction of a CNF.[35] As a result, the chemical strain ε^{c}_{ij} in *d*-C is similarly assumed to be highly anisotropic with only one nonzero component in the radial direction. In addition, because the longitudinal elongation of the CNFs is negligibly small in TEM experiments, the plane strain condition is assumed in the axial direction.

Finite element simulations based on the above chemomechanical model predict the geometrical changes in sodiated bilayer CNFs (Figure 5a,b) that agree with experimental measurements. From the experimental data of volumetric chemical strains (being 6.0 and 18.7% in *c*-C and *d*-C layers, respectively) and considering the anisotropic nature of chemical strains as discussed above, we take $\varepsilon_r^{c,c\text{-C}} = 0.06$, $\varepsilon_\theta^{c,c\text{-C}} = \varepsilon_z^{c,c\text{-C}} = 0$ for *c*-C, and $\varepsilon_r^{c,d\text{-C}} = 0.187$, $\varepsilon_\theta^{c,d\text{-C}} = \varepsilon_z^{c,d\text{-C}} = 0$ for *d*-C. In our simplified elastic model, the radial displacement depends on Poisson's ratio ($\nu = 0.2$), but is independent of Young's modulus.[36] The solid line in Figure 5b shows the predicted radial displacement u_r as a function radial distance *r*. It is seen that u_r is negative in the *c*-C layer and so is u_r at the *c*-C/*d*-C interface. In the *c*-C layer, u_r becomes positive with increasing *r* and reaches the maximum at the outer surface of the tube. These modeling results are consistent with the experimental measurements (circles in Figure 5b), and their numerical differences arise possibly due to a neglect of plastic strains in our model. It should be noted that previous studies have emphasized the critical role of chemical strain anisotropy in stress generation.[36−38] This work also supports the notation of anisotropic chemical strain, which results from the layered graphene lattice. At the moment of this study, the stress in the system cannot be quantitatively predicted, because the in situ TEM setup is incapable of measuring the mechanical properties of nanosized electrodes.

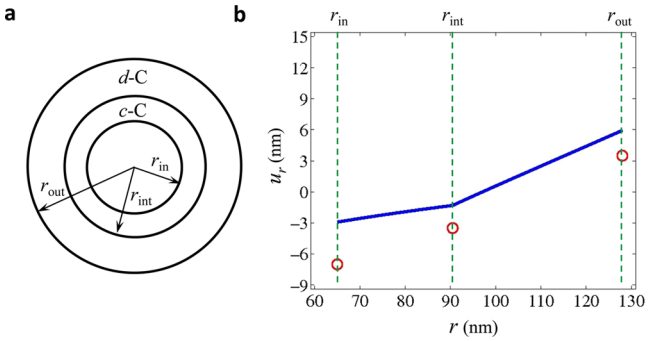

Figure 5. Chemomechanical modeling of sodiation-induced geometrical changes in a hollow bilayer CNF. (a) Schematic of cross section of the tube before sodiation, where r_{in} and r_{out} are respectively the inner and outer radius of the tube, and r_{int} is the radius of the *c*-C/*d*-C interface. (b) Predicted radial displacement u_r versus radial distance *r* (solid line), compared with experimental data (circles) .

To further understand the coupling between mechanical and electrochemical responses in CNFs, the sodiation behavior of an *a*-Si coated CNF (*a*-Si/CNF) is also investigated, as shown in Figure 6 and Supporting Information Figure S5. The *a*-Si layer is coated on the outer surface of the CNF with a thickness of ∼19 nm (Figure 6a,d). Because of geometrical confinement of the stiff *a*-Si coating, the sodiated bilayer tends to expand inward to the hollow space of the CNF, resulting in a large decrease of the inner tube diameter (Figure 6b). Similar to the case without coating, sodiation also leads to crack formation along the longitudinal direction of the *a*-Si/CNF (Figure 6c), and cracking occurs near the *c*-C/*d*-C interface (Supporting Information Figure S5). Note that the thickness of the *a*-Si coating remains unchanged during sodiation, indicating negligible Na insertion in *a*-Si. This is further confirmed by EDPs of the *a*-Si/CNF before and after sodiation (Figure 6f,g). The sodiated CNF shows a typical split EDP, while no change is observed in the diffraction rings of *a*-Si before and after sodiation. These in situ TEM results suggest that nanoscale *a*-Si may not be a viable anode material for NIBs. A previous theoretical study indicates that Si may serve as an anode material for NIBs,[8] despite the lack of direct experimental support to date.[15] Our in situ TEM study indicates that *a*-Si is electrochemically unfavorable for NIBs. Moreover, the surface coating of *d*-C or amorphous C has been widely used to enhance the electronic conductivity or serve as a structural support for nanocomposite electrodes of NIBs.[24−27] The present sodiation study of *a*-Si/CNF also suggests that even when *d*-C is covered with an inactive surface layer, it can still be effectively sodiated or potassiated, likely due to the fast diffusion of Na and K ions at the interface.

In conclusion, the electrochemical reactions and associated structure changes of hollow bilayer CNFs during sodiation and potassiation have been studied by in situ TEM. It is shown that *d*-C exhibits about three times the volume expansion of *c*-C, thus indicating a larger Na or K ion storage capability in *d*-C than *c*-C. Longitudinal cracks are frequently observed near the *c*-C/*d*-C interface after sodiation and potassiation. An unexpected shrinkage of the inner tube is explained in terms of anisotropic sodiation strains in *c*-C and *d*-C. Moreover, the sodiation study of

dx.doi.org/10.1021/nl500970a | *Nano Lett.* 2014, 14, 3445−3452

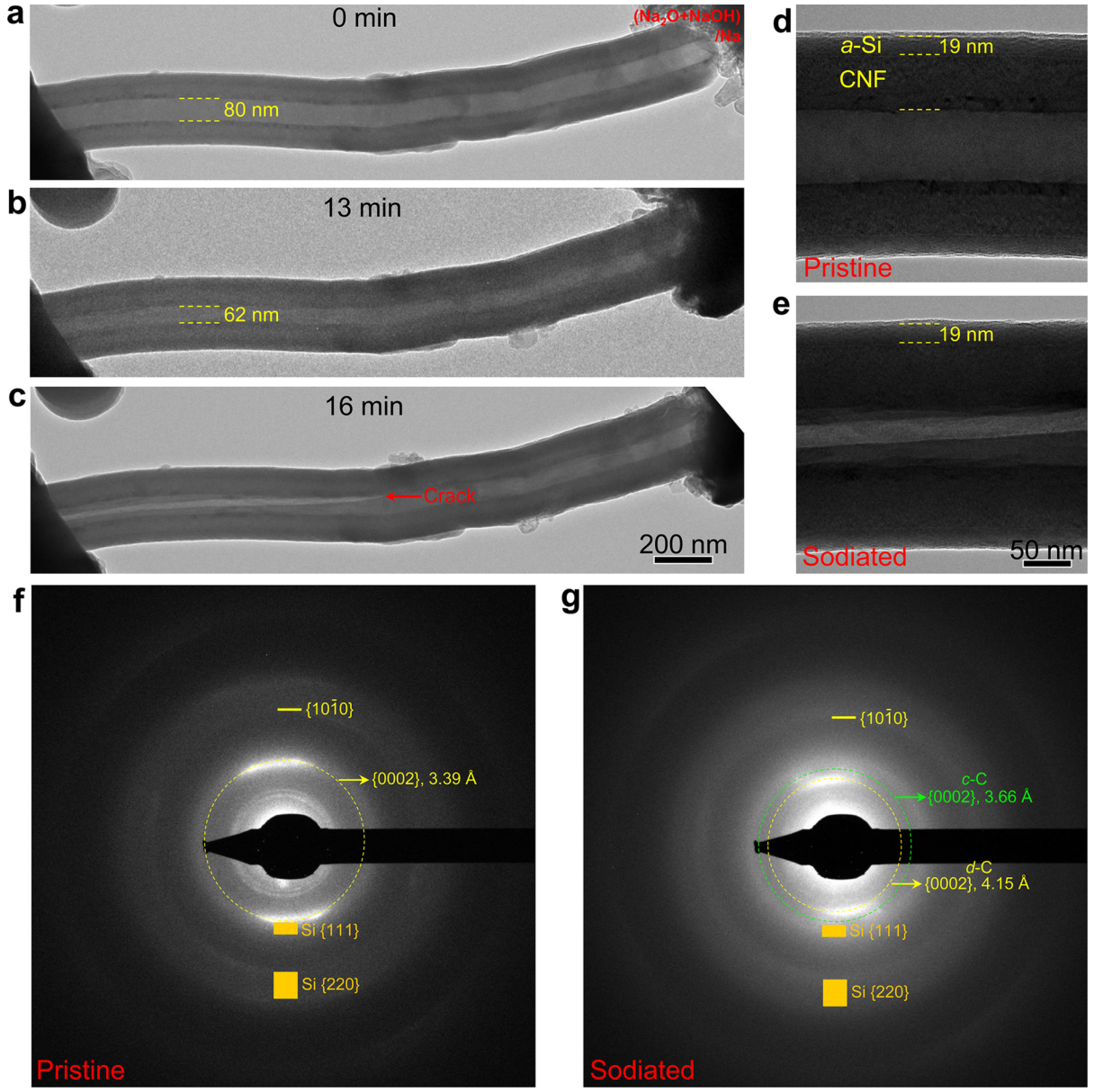

Figure 6. Structure changes of an amorphous silicon-coated CNF (*a*-Si/CNF) before and after sodiation. (a,d) A pristine CNF with *a*-Si coating (~19 nm in thickness). The diameter of the inner wall is about 80 nm. (b) Upon sodiation, the diameter of the inner wall gradually reduces due to the geometric confinement of the stiff *a*-Si coating, and it decrease to ~62 nm at the moment of crack formation. (c,e) The crack finally forms along the longitudinal direction of the *a*-Si/CNF system. The thickness of the *a*-Si coating does not change after sodiation, indicating no reaction occurs. (f,g) EDPs of the pristine and sodiated *a*-Si/CNF. The sodiated CNF exhibits a typical split EDP, while no change is observed in the diffraction rings of *a*-Si before and after sodiation, confirming no reaction occurs in *a*-Si.

a-Si/CNFs demonstrates that the nanoscale *a*-Si is not a viable anode material for NIBs. Our work suggests that disordered-carbon holds great promise in applications for NIBs and KIBs. The in situ TEM results provide critical insight into the electrochemical reaction and degradation mechanisms of the carbon-based anodes for NIBs and KIBs.

■ ASSOCIATED CONTENT

Supporting Information

The supporting figures showing the sodiation- and potassiation-induced cracks in CNFs under beam blank, as well as sodiation-induced cracks in *a*-Si/CNF. This material is available free of charge via the Internet at http://pubs.acs.org.

■ AUTHOR INFORMATION

Corresponding Authors

*E-mail: ting.zhu@me.gatech.edu.
*E-mail: cswang@umd.edu.

Author Contributions

Y.L., F.F. and J.W. contributed equally to this work.

Notes

The authors declare no competing financial interest.

■ ACKNOWLEDGMENTS

We acknowledge the support of the Maryland Nano Center and its NispLab. T.Z. acknowledges the support of the NSF Grant CMMI-1100205. In addition, this work was performed, in part, at the Center for Integrated Nanotechnologies, a U.S. Department

of Energy, Office of Basic Energy Sciences user facility. Sandia National Laboratories is a multiprogram laboratory managed and operated by Sandia Corporation, a wholly owned subsidiary of Lockheed Martin Corporation for the U.S. Department of Energy's National Nuclear Security Administration under Contract DE-AC04-94AL85000.

REFERENCES

(1) Chan, C. K.; Peng, H.; Liu, G.; McIlwrath, K.; Zhang, X. F.; Huggins, R. A.; Cui, Y. *Nat. Nanotechnol.* **2008**, *3*, 31−35.
(2) Etacheri, V.; Marom, R.; Elazari, R.; Salitra, G.; Aurbach, D. *Energy Environ. Sci.* **2011**, *4*, 3243−3262.
(3) Slater, M. D.; Kim, D.; Lee, E.; Johnson, C. S. *Adv. Funct. Mater.* **2013**, *23*, 947−958.
(4) Tang, K.; Fu, L.; White, R. J.; Yu, L.; Titirici, M.-M.; Antonietti, M.; Maier, J. *Adv. Energy Mater.* **2012**, *2*, 873−877.
(5) Wessells, C. D.; Peddada, S. V.; Huggins, R. A.; Cui, Y. *Nano Lett.* **2011**, *11*, 5421−5425.
(6) Lee, K. T.; Hong, S. Y.; Kim, Y.; won Park, Y.; Choi, A.; Choi, N.-S. *Energy Environ. Sci.* **2013**, *6*, 2067−2081.
(7) Palomares, V.; Casas-Cabanas, M.; Castillo-Martinez, E.; Han, M. H.; Rojo, T. *Energy Environ. Sci.* **2013**, *6*, 2312−2337.
(8) Chevrier, V. L.; Ceder, G. *J. Electrochem. Soc.* **2011**, *158*, A1011−A1014.
(9) Ellis, L. D.; Hatchard, T. D.; Obrovac, M. N. *J. Electrochem. Soc.* **2012**, *159*, A1801−A1805.
(10) Wang, J. W.; Liu, X. H.; Mao, S. X.; Huang, J. Y. *Nano Lett.* **2012**, *12*, 5897−5902.
(11) Xiong, H.; Slater, M. D.; Balasubramanian, M.; Johnson, C. S.; Rajh, T. *J. Phys. Chem. Lett.* **2011**, *2*, 2560−2565.
(12) Cao, Y.; Xiao, L.; Wang, W.; Choi, D.; Nie, Z.; Yu, J.; Saraf, L. V.; Yang, Z.; Liu, J. *Adv. Mater.* **2011**, *23*, 3155−3160.
(13) Alcántara, R.; Jiménez-Mateos, J. M.; Lavela, P.; Tirado, J. L. *Electrochem. Commun.* **2001**, *3*, 639−642.
(14) Alcántara, R.; Lavela, P.; Ortiz, G. F.; Tirado, J. L. *Electrochem. Solid-State Lett.* **2005**, *8*, A222−A225.
(15) Cao, Y.; Xiao, L.; Sushko, M. L.; Wang, W.; Schwenzer, B.; Xiao, J.; Nie, Z.; Saraf, L. V.; Yang, Z.; Liu, J. *Nano Lett.* **2012**, *12*, 3783−3787.
(16) Komaba, S.; Murata, W.; Ishikawa, T.; Yabuuchi, N.; Ozeki, T.; Nakayama, T.; Ogata, A.; Gotoh, K.; Fujiwara, K. *Adv. Funct. Mater.* **2011**, *21*, 3859−3867.
(17) Wenzel, S.; Hara, T.; Janek, J.; Adelhelm, P. *Energy Environ. Sci.* **2011**, *4*, 3342−3345.
(18) Zhao, J.; Zhao, L.; Chihara, K.; Okada, S.; Yamaki, J.-i.; Matsumoto, S.; Kuze, S.; Nakane, K. *J. Power Sources* **2013**, *244*, 752−757.
(19) Stevens, D.; Dahn, J. *J. Electrochem. Soc.* **2000**, *147*, 1271−1273.
(20) Scrosati, B. *Electrochim. Acta* **2000**, *45*, 2461−2466.
(21) Stevens, D.; Dahn, J. *J. Electrochem. Soc.* **2001**, *148*, A803−A811.
(22) Shao, Y.; Xiao, J.; Wang, W.; Engelhard, M.; Chen, X.; Nie, Z.; Gu, M.; Saraf, L. V.; Exarhos, G.; Zhang, J.-G.; Liu, J. *Nano Lett.* **2013**, *13*, 3909−3914.
(23) Kim, Y.; Park, Y.; Choi, A.; Choi, N.-S.; Kim, J.; Lee, J.; Ryu, J. H.; Oh, S. M.; Lee, K. T. *Adv. Mater.* **2013**, *25*, 3045−3049.
(24) Qian, J.; Chen, Y.; Wu, L.; Cao, Y.; Ai, X.; Yang, H. *Chem. Commun.* **2012**, *48*, 7070−7072.
(25) Xiao, L.; Cao, Y.; Xiao, J.; Wang, W.; Kovarik, L.; Nie, Z.; Liu, J. *Chem. Commun.* **2012**, *48*, 3321−3323.
(26) Zhu, Y.; Han, X.; Xu, Y.; Liu, Y.; Zheng, S.; Xu, K.; Hu, L.; Wang, C. *ACS Nano* **2013**, *7*, 6378−6386.
(27) Zhu, Y.; Wang, J. W.; Liu, Y.; Liu, X.; Kushima, A.; Liu, Y.; Xu, Y.; Mao, S. X.; Li, J.; Wang, C.; Huang, J. Y. *Adv. Mater.* **2013**, *25*, 5461−5466.
(28) Wang, J. W.; He, Y.; Fan, F.; Liu, X. H.; Xia, S.; Liu, Y.; Harris, C. T.; Li, H.; Huang, J. Y.; Mao, S. X. *Nano Lett.* **2013**, *13*, 709−715.
(29) Wang, J. W.; Liu, X. H.; Zhao, K.; Palmer, A.; Patten, E.; Burton, D.; Mao, S. X.; Suo, Z.; Huang, J. Y. *ACS Nano* **2012**, *6*, 9158−9167.
(30) Liu, Y.; Zheng, H.; Liu, X. H.; Huang, S.; Zhu, T.; Wang, J.; Kushima, A.; Hudak, N. S.; Huang, X.; Zhang, S.; Mao, S. X.; Qian, X.; Li, J.; Huang, J. Y. *ACS Nano* **2011**, *5*, 7245−7253.
(31) Liu, X. H.; Wang, J. W.; Liu, Y.; Zheng, H.; Kushima, A.; Huang, S.; Zhu, T.; Mao, S. X.; Li, J.; Zhang, S.; Lu, W.; Tour, J. M.; Huang, J. Y. *Carbon* **2012**, *50*, 3836−3844.
(32) Liu, X. H.; Wang, J. W.; Huang, S.; Fan, F.; Huang, X.; Liu, Y.; Krylyuk, S.; Yoo, J.; Dayeh, S. A.; Davydov, A. V. *Nat. Nanotechnol.* **2012**, *7*, 749−756.
(33) Zhou, X.; Guo, Y.-G. *ChemElectroChem* **2014**, *1*, 83−86.
(34) Liu, X. H.; Liu, Y.; Kushima, A.; Zhang, S. L.; Zhu, T.; Li, J.; Huang, J. Y. *Adv. Energy Mater.* **2012**, *2*, 722−741.
(35) Thomas, P.; Billaud, D. *Electrochim. Acta* **2001**, *46*, 3359−3366.
(36) Hsueh, C. H.; Evans, A. G. *J. Appl. Phys.* **1983**, *54*, 6672−6686.
(37) Huang, S.; Fan, F.; Li, J.; Zhang, S. L.; Zhu, T. *Acta Mater.* **2013**, *61*, 4354−4364.
(38) Liang, W.; Yang, H.; Fan, F.; Liu, Y.; Liu, X. H.; Huang, J. Y.; Zhu, T.; Zhang, S. *ACS Nano* **2013**, *7*, 3427−3433.